ORIGINAL RESEARCH

Cellulose nanofiber-reinforced dissolving microneedles for transdermal delivery of a water-soluble compound

Jin Ah Kim · Soo Chan Park · Seung-Jun Lee · Jin-Chul Kim

Abstract Cellulose nanofibers (CNFs) were included in dissolving microneedle (MN) arrays to increase needle stiffness and control the dissolving rate and transdermal delivery rate. A metallic MN master was fabricated to build pyramidal needles in a 15×15 array using a pre-fabricated silicone mold as a template. The dissolving MNs with different CNF contents were replicated by casting the polymeric mixtures on the molds. X-ray diffraction study revealed that CNFs were included in the MN arrays with maintaining its crystalline structure. The compressive strength test showed that the addition of CNFs increased the stiffness of the needles, and the needles underwent the elastic deformation, the failure of the tip, and the elastic deformation of stem. The skin-piercing capability of the MNs was enhanced by including CNFs in the MN arrays. Once the needles penetrated into the skin, the depth was almost the same, regardless of CNF content. As CNF content increased, the release rate of a water-soluble cargo loaded in the MNs, the dissolution rate of the MNs, and the in vitro transdermal delivery rate of the cargo decreased, possibly because CNFs would form networks within the MNs through physical entanglement and/or hydrogen bonding.

Keywords Cellulose nanofiber · Microneedles · Stiffness · Skin-piercing capability · Transdermal delivery

Jin Ah Kim and Soo Chan Park have contributed equally to this work.

J. A. Kim · S. C. Park · J.-C. Kim (✉)
Department of Biomedical Science & Institute of Bioscience and Biotechnology, Kangwon National University, Chuncheon 24341, Republic of Korea
e-mail: jinkim@kangwon.ac.kr

S.-J. Lee
Department of Pharmaceutical Science and Engineering, Seowon University, 377-3, Musimseoro, Seowon-gu, Cheongju, Chungbuk 28674, Republic of Korea

Introduction

Microneedles (MNs) are structures with tiny needles built on the substrate that are developed for dermal and transdermal delivery of drugs (Mittapally et al. 2018; Ye et al. 2018; Yin et al. 2018; Waghule et al. 2019). The structures are fabricated using microelectronics and micromachinery techniques so that the diameter is in the order of microns and the length is hundreds of micrometers. MNs can pierce the stratum corneum in a non-invasive manner without pain to deliver drugs effectively into the skin for both local and systemic effects. MNs with different geometries have been fabricated as solid and hollow types using various materials from polymers to metals (Sharma et al. 2019). MNs deliver drugs into the skin in four ways (Prausnitz 2004; van der Maaden et al. 2012; Benson et al. 2019). "Poke and flow" is a delivery way where hollow MNs are applied to the skin,

and drugs are allowed to flow into the skin. "Poke and patch" is a way where drugs are applied on the pierced skin after MNs are removed. In the "Poke and release" delivery method, porous and dissolving MNs are applied to the skin, and drugs are allowed to release into the skin. "Coat and poke" is an approach where MNs are coated with drugs before applying them to the skin. The latter three approaches can be accomplished by solid MNs.

Studies suggest that a variety of drugs, such as parathyroid hormone, insulin, influenza vaccine, lidocaine, dyclonine, rabies vaccine, and naltrexone, can be loaded in the MNs for dermal and transdermal delivery in humans (Daddona et al. 2011; van der Maaden et al. 2012; Koutsonanos et al. 2013; Quinn et al. 2014). However, the optimization of the MN type is of utmost importance for its practical use. Moreover, hollow, solid, geometry, material, density, and length should also be chosen or designed carefully for the high therapeutic efficacy of drugs loaded in MNs (Prausnitz 2004; Lee et al. 2008; van der Maaden et al. 2012). In addition, one of the requirements of MNs to be used for dermal and transdermal delivery is that they should be mechanically strong enough to pierce the skin without breaking down (Park et al. 2005; Sullivan et al. 2008). Otherwise, MNs could hardly pierce the skin to administer the required dose in a reproducible way.

It was reported that the force required to penetrate human skin is 0.08 N/needle (Davis et al. 2004). Jiang and Lillehoj (2020) successfully developed a hollow MN array made from polymerized SU-8 photoresist on a flexible polyethylene terephthalate (PET) substrate for blood-free diagnostic testing. They observed that in the force–displacement test of the microneedle arrays under mechanical compression, some deformation of the microneedles occurred around 0.2 N/needle, much higher than the criterion for human skin perforation (i.e. 0.08 N/needle) and the microneedles could penetrate cadaver porcine skin successfully. Another proposed criterion for the skin perforation was that needles with below a 12:1 aspect ratio of length-to-equivalent diameter and more than 3 GPa of Young's modulus should be used for reducing sudden failure by buckling and for successfully inserting the needle into the skin (Park and Prausnitz 2010).

In a previous study, an array of dissolving MNs containing magnesium ascorbyl phosphate (MAP) was prepared in order to investigate the effect of the MAP content on the compressive strength of the needles, the in vitro toxicity, and the in vitro skin permeation of MAP (Kim et al. 2021). A marked increase in the stiffness of the needles was observed without an appreciable decrease in the failure load when MAP was included in the MN array at the content of 7.5%. At all the MAP contents tested (i.e., 7.5, 14, and 24.5%), there was no severe toxicity once the concentration of the constituents of the MN arrays was less than 100 µl/ml. These MNs could promote skin permeation effectively, whereas MAP could hardly permeate the skin when applied as a solution.

In this study, cellulose nanofibers (CNFs) were included in dissolving MN arrays to increase the stiffness of the needles and to control the dissolving rate and the transdermal delivery rate. CNFs are nanostructured cellulose fibrils that are in abundant, naturally occurring biomass. The lengths of CNFs are on the order of micrometers, and their diameter is about 10–100 nm. CNFs contain both crystalline and amorphous cellulose domains (Tejado et al. 2012; Dufresne 2017). Owing to the axial rigidity (Kiziltas et al. 2016; Wang et al. 2018), CNFs are thought to enhance the stiffness of a dissolving polymeric MNs. In addition, CNFs would be able to form networks through physical entanglement and/or hydrogen bonding among its strands, leading to the formation of stiff MNs. The MN arrays were fabricated by casting the mixture aqueous solution of CNF, a polysaccharide (i.e., hyaluronic acid), a protein (i.e., collagen), and sugar (i.e., trehalose) on a silicone mold and drying it at room temperature. The compressive strength of the needles was measured at varying CNF content. The mechanical properties of the needles, including Yong's modulus and tip failure strength, were compared with the previously reported data to appreciate whether they fell within the criteria for skin penetration. The release profiles of a fluorescence dye (i.e., calcein) loaded in the MN arrays were investigated using phosphate-buffered saline (PBS; 10 mM, pH 7.4) as a release medium. The in vitro skin permeation of the dye loaded in the MN arrays was observed using a diffusion cell and an artificial skin. The skin-penetrating capability of the needles was estimated by observing the needles penetrated into the skin on a fluorescence microscope and counting the number of pierced holes on the skin.

Table 1 The mass and the mass percent of each component contained in mixture solutions (S/MN0, S/MN1, S/MN2, and S/MN3) for the preparation of MN arrays (MN0, MN1, MN2, and MN3)

	CNF (g/%)	HA (g/%)	Collagen (g/%)	Trehalose (g/%)	Total solid content (g/%)	DW (ml)
S/MN0	0/0	0.3 /48.8	0.3/48.8	0.015/2.4	0.615/100	10
S/MN1	0.02/3.3	0.2903/47.6	0.2903/47.6	0.0145/2.4	0.615/100	10
S/MN2	0.1/16	0.2512/41	0.2512/41	0.0126/2	0.615/100	10
S/MN3	0.2/32.5	0.2024/32.9	0.2024/32.9	0.0101/1.6	0.615/100	10

Experimental section

Materials

Hyaluronic acid (HA) was purchased from SK Bioland Co., Ltd. (Cheonan, Korea). Collagen peptide (Collagen) was purchased from CNA Biotech., Co., Ltd. (Chungbuk, Korea). Trehalose, calcein, and PBS were purchased from Sigma–Aldrich Co. (St. Louis, MO, USA). Pristine cellulose nanofibers (CNFs) prepared by a supermass colloider were purchased from Cellulose-Lab (Canada). The width is 30–80 nm, the length is > 100 μm, the surface functional group is hydroxyl, and the surface is almost electrostatically neutral (Fularz et al. 2022). A silicone rubber solution (poly(dimethylsiloxane) (PDMS), ELASTOSILR RT623 A), a silicone hardening agent (a cross-linker, ELASTOSILR RT623 B), and a silicone oil (a softening agent, AK35(C)) were obtained from Wacker Chemicals Korea Inc. Strat-M® Membrane (Transdermal Diffusion Test Model, 25 mm) was purchased from Millipore (Billerica, MA, USA) as an artificial skin. It is a synthetic, non-animal-based model for transdermal diffusion testing that is claimed to be predictive of diffusion in human skin (Ossowicz-Rupniewska et al 2021).

Fabrication of master and mold

A metal master was fabricated by a micromachinery technique (EHWA Diamond Ltd, Korea) (Xu et al. 2013). A silicone rubber solution (PDMS, ELASTOSILR RT623 (A)), a silicone hardening agent (a cross-linker, ELASTOSILR RT623 (B)), and a silicone oil (a softening agent, AK35 (C)) were mixed in a mass ratio of 9:1:3. The microneedle (MN) master was placed in the center of a Petri dish (35 mm in diameter), the silicone mixture solution was poured into the dish until the master was completely immersed, then the dish containing the master and the silicone mixture solution was stored at an oven thermostated at 60 °C for 4 h for the solidification of silicone solution. The PDMS mold was peeled off the dish and the master.

Preparation of MN arrays

CNFs were dispersed in 10 ml of distilled water, and then HA, collagen, and trehalose were co-dissolved in the CNF suspension to prepare MN arrays incorporating CNFs. The mass and the mass percent of each component contained in mixture solutions to prepare MN arrays were summarized in Table 1. S/MN0 was a mixture solution without CNFs. S/MN1, S/MN2, and S/MN3 were mixture solutions whose CNF concentrations were different from one another while total solid concentrations were the same. 0.7 g each of mixture solutions was evenly applied onto the surface of a MN mold and was centrifuged at 4,500 rpm (3736 g) for 3 min on a centrifuge (rotor 13, NB-550, N-BIOTEK, Korea) to fill the pyramidal pore of the mold with the solution. The molded mixture solution on the mold was dried in a desiccator for two days to form a MN array, which was subsequently detached from the mold carefully. The MN arrays prepared from a mixture solution of S/MN0, 1, 2, and 3 were called MN0, 1, 2, and 3, respectively.

Scanning electron microscopy

Each of the MN arrays was placed on a metal stub and sputtered with gold for the surface coating. Then, the surface topologies of the MN arrays were investigated on a scanning electron microscope (SEM, S-4800, Hitachi, located at the Central Laboratory of Kangwon National University).

X-ray diffraction spectroscopy

The crystalline structure of MN0, MN1, MN2, MN3, and CNFs were examined by X-ray diffraction (XRD) on a XRD diffractometer (X'Pert PRO MPD). X-ray sources were Cu Kα1 radiation ($\lambda = 1.5506$ Å) and Cu Kα2 radiation ($\lambda = 1.5444$ Å), and the ratio of Kα2/Kα1 was 0.5. 2 θ range was 5–45°, scan range 5, scan step size 0.0131303, divergence slit 1.52 nm, and generator voltage 40 kV.

Measurement of compressive strength

The compressive force profile versus strain was investigated to understand the mechanical strength of MNs against the compressive force which was applied on MN array. Each MN arrays was cut into a square patch containing 15×15 needles and placed on the center of the load cell (UMN-K10, Dacell, Korea) of a universal testing machine (TO-100-IC, Testone Co., Korea). Force imposed on the MN arrays was recorded up to a maximum force of 1.078 N while the load cell was moving up to an upper stationary plate at a constant rate of 0.2 mm/min. The compressive force profiles were obtained by plotting the force imposed on the MN array versus strain. The compressive forces at a displacement (ca. 30 μm) where the needles exhibiting the highest Young's modulus (i.e. MN2) began to undergo their tip failure were statistically analyzed by Student's t test, and the statistical significance was evaluated at $p < 0.001$, $p < 0.05$, and $p < 0.1$. The SEM micrographs of MN arrays were taken using the same method described above after they were subjected to a compressive strength test.

Skin-piercing capability of MNs

Each MN arrays was separately placed at the center of an artificial skin (Start-M®Membrane, Transdermal Diffusion Test Model, 25 mm) with the needles facing the skin surface. The surface of MN array was pressed for 5 s using a disc plate (1.5 cm in diameter) so that 14.7 N of compressive force was evenly applied on the surface of MN array. After the MN array was removed from the skin, 100 μl of trypan blue was spread on the skin to visualize perforated holes more clearly, and the dyed skin was dried at room temperature for 12 h. The micrograph of the perforated skin was taken using a portable microscope

(ViTiny UM12, Oasis Scientific Inc, USA). The perforation degree (%) was defined as the percent of the number of the perforated holes based on the number of MNs (Cha et al. 2014; Jeong et al. 2018).

Skin-penetrating capability of MNs

Each of the calcein-loaded MN arrays was separately placed at the center of an artificial skin (Start-M®Membrane, Transdermal Diffusion Test Model, 25 mm) with the needles facing the skin surface. The surface of the MN array was pressed using a disc plate (1.5 cm in diameter) so that 14.7 N of compressive force was evenly applied on the surface of the MN array. The MN array-attached skin was cut along the row of the needles, and the cross-sections were observed on an optical microscope and a fluorescence microscope (DMi8, Leica, Germany).

Release of fluorescence dye from MN array

Each of the MN arrays containing calcein was immersed in 5 ml of PBS (10 mM, pH 7.4) contained in a Petri dish (35 mm in diameter), capped with a lid, and stored in an oven thermostated at 32 °C. Then, 2 ml of medium was taken at pre-determined time points for 120 min to determine the fluorescence intensity of calcein at 515 nm using the excitation wavelength of 495 nm on a fluorescence spectrophotometer (F2500, Hitachi, Japan). The medium was transferred back to the Petri dish to keep the volume of release medium constant. The release % was defined as the percent of the amount of dye released based on the initial amount of dye loaded in a MN array. In parallel, the photographs of MN arrays in the buffer solution (32 °C) were taken at a given time to observe the dissolving property.

In vitro skin permeation

Each MN arrays was placed in the center of an artificial skin (Start-M®Membrane, Transdermal Diffusion Test Model, 25 mm), and 14.7 N of compressive force was evenly applied on the array so the needles could pierce the skin. The MN array-attached skin was mounted onto a Franz diffusion cell (0.636 cm^2 in surface area). The receptor cell was filled with 5 ml of PBS (10 mM, pH 7.4) and thermostated at 32 °C. In parallel, 0.7 ml of calcein solution (0.1 mM, in PBS

(10 mM, pH 7.4)) was applied to the skin as a control compared to the MN array. Then, 2 ml of receptor solution was taken at a given time for 24 h, and the fluorescence intensity was determined at 515 nm with being excited at 495 nm on a fluorescence spectrophotometer (F2500, Hitachi, Japan). After measuring the fluorescence intensity, it was put back into the receptor cell to keep the volume of the receptor solution constant. The amount of dye was calculated using a calibration curve. The skin permeation degree of dye was expressed as the cumulative amount of dye permeated through the unit area of the skin.

Results and discussion

Fabrication of master and mold

Figure 1 shows the photomicrograph of a tungsten MN master. Pyramidal needles were built on the square base (1.5 cm X 1.5 cm) in 15×15 array, being equally spaced by 700 µm. The base width and the height of each metallic needle were 300 µm and 600 µm, respectively. Figure 2 shows the photomicrograph of a PDMS mold. On the top view photomicrograph (Fig. 2a), a 15×15 array of square holes was shown whose dimensions were almost the same as the base width of the needles of the master (i.e., 300 µm). On the cross-sectional view photomicrograph (Fig. 2b), conical holes were shown whose width and depth were close to the base width (i.e., 300 µm) and the height (i.e., 600 µm) of the needles of the master. Since the dimension of the holes was almost the same as that of the needles of the master, it could be said that the silicone solution was evenly spread and distributed throughout the Petri dish containing the master and the mold was successfully fabricated.

Preparation of MN arrays

Figure 3 shows the SEM micrograph of MN0, MN1, MN2, and MN3. The top view micrograph of each MN arrays showed pyramidal needles as squares due to their four base sides. They exhibited four white lines within the squares due to another four inclined sides, and they were arrayed in the same pattern as the needles of the master. The side view micrograph of each MN arrays showed that the needles were pyramid-shaped, with a base width of about 300 µm. The
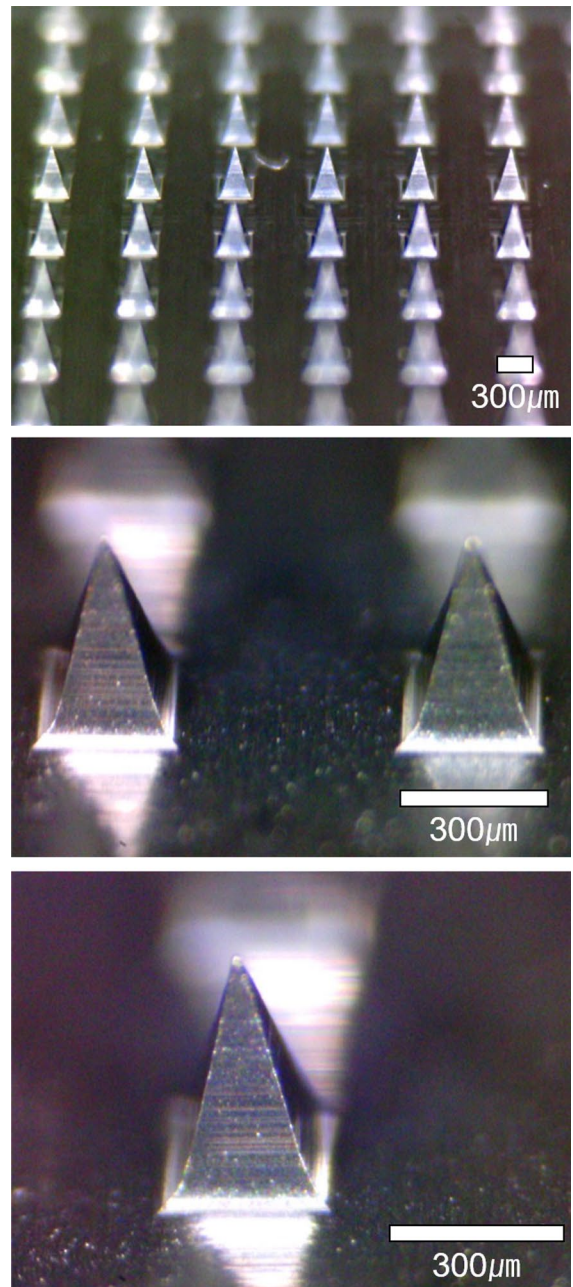
Fig. 1 Photomicrograph of a tungsten MN master

shape and the dimension of replicated needles were almost the same as those of the needles of the master, indicating that the MN arrays were successfully duplicated from their master. The marked difference in the appearance among the MN arrays was the surface was rougher as CNF content was higher. CNFs

Fig. 2 Photomicrograph of a PDMS mold. 15×15 array of square holes were shown on top view photomicrograph (**a**). Conical holes were shown on cross-sectional view photomicrograph (**b**)
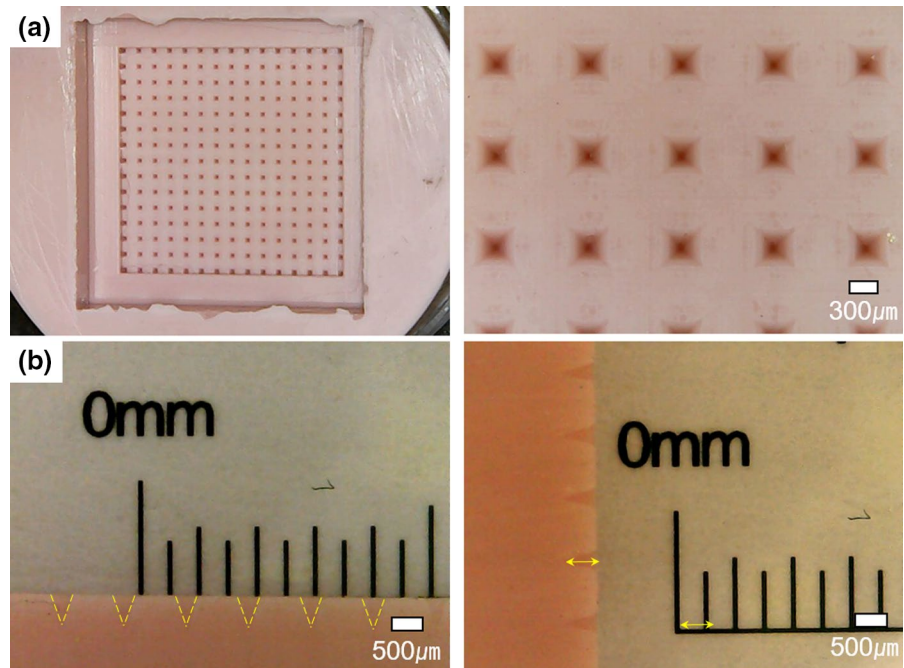
were included in MN0, MN1, MN2, and MN3 so that the content was 0, 3.3, 16, and 33%, respectively.

Since HA, collagen, and trehalose were readily dissolved in water, the mixture solution (i.e., S/MN0) would be homogeneous at a molecular level. Hence, it would be able to produce a smooth surface if water was evaporated after being cast. On the other hand, CNFs are not single molecules but a bundle of cellulose molecules with the length in several hundred micrometers and the diameter of about 30–80 nm. Owing to such a large dimension, the mixture solutions containing CNFs (i.e., S/MN1, S/MN2, S/MN3) would hardly produce a smooth surface upon casting and drying, even if the fibers were well-dispersed in an aqueous solution. The strands of CNFs would be entangled due to their long length and they would form clusters, giving rise to a casting film with a rough surface.

X-ray diffraction spectroscopy

Figure 4 shows the XRD spectrum of MN0, MN1, MN2, MN3, and CNFs. In the spectrum of CNFs, diffraction peaks corresponding to the (110) plane, the (200) plane, and the (004) plane of cellulose crystalline structure were found at 2θ of 15.8°, 22.6 °, and 34.4 °, respectively (Chen et al. 2011; Kumar

et al. 2020). In the spectrum of MN0, no characteristic peaks were found, indicating that the MN array was amorphous. In fact, hyaluronic acid and collagen (the major components of MN0) are known to be almost amorphous polymers (Kozlov and Burdygina 1983; Zaupa et al. 2010). No characteristic peaks were found either in the spectrum of MN1, possibly because the content of CNFs (3.3%) was too small to be detected. In the spectrum of MN2, the characteristic peak was found at 2θ of 22.2°, due to the diffraction from the (200) plane of the crystalline structure of CNFs. In the spectrum of MN3, the characteristic peak at 2θ of 22.5° was more prominent and the peaks at 2θ of 15.7° and 34.5°, signals from the (110) and (004) planes of crystalline CNFs, respectively. Thus, the results obtained by XRD suggested that the diffraction intensity became stronger as the content of CNFs increased and that CNFs was included in the MN arrays with maintaining its crystalline structure.

Measurement of compressive strength

Figure 5 shows the compressive force profiles of MN0, MN1, MN2, and MN3. In the compressive force profile of MN0, the compressive force obtained immediately after the MN array came in contact with the stationary plate was about 0.1078 N. It was
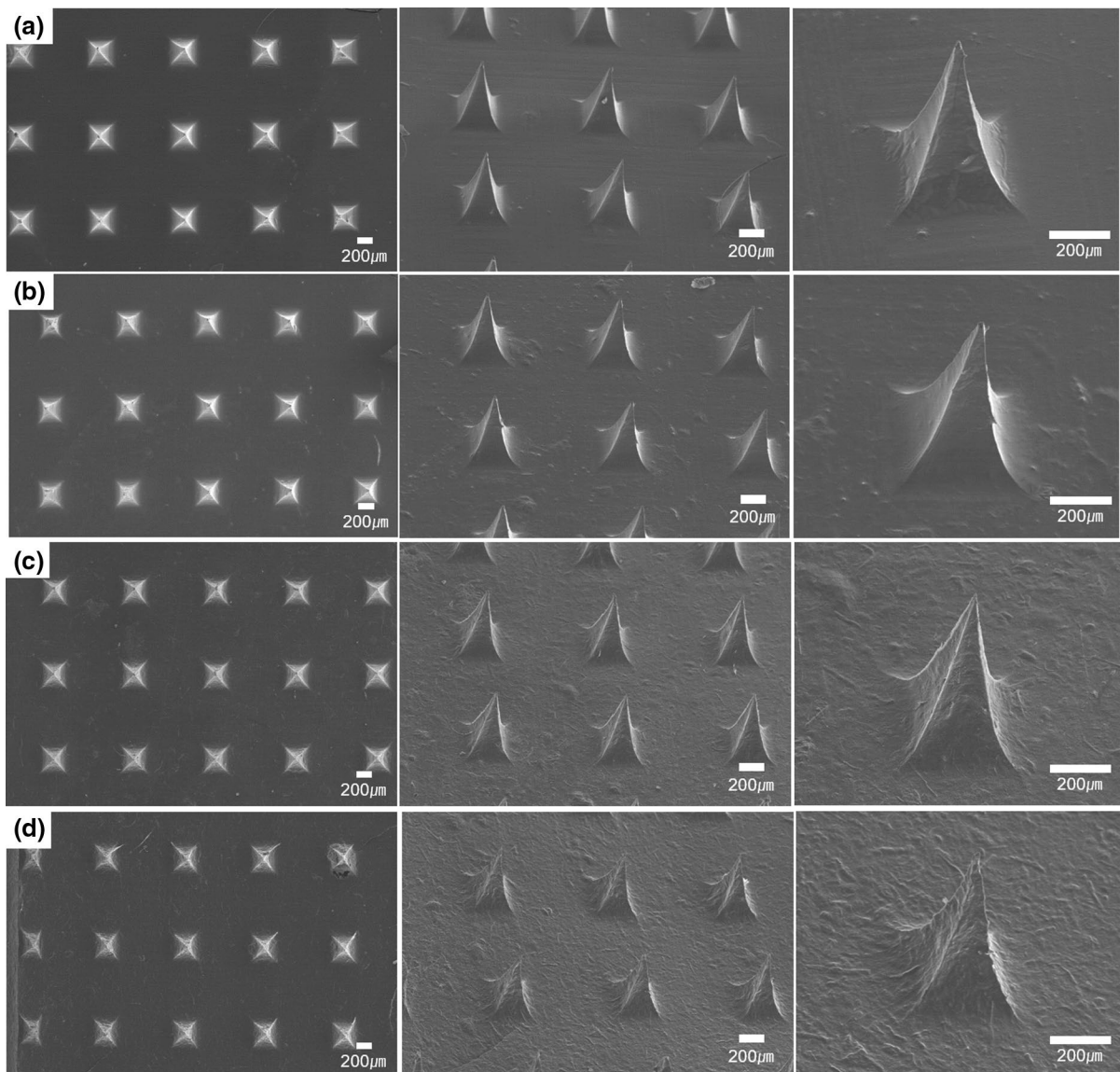
Fig. 3 SEM micrograph of MN0 (**a**), MN1 (**b**), MN2 (**c**), and MN3 (**d**)

observed that the compressive force of MN array increased linearly up to 0.4018 N when the strain increased to 125 μm. Further, the compressive force of the MN array was almost constant when the strain ranged between 125 and 200 μm, and increased again with increasing strain. The first strain of 0–125 μm was thought to be the elastic deformation of needles because the compressive force increased with strain almost linear. The second strain of 125–200 μm would be due to the needle failure because no significant force was required to cause such a marked

strain. Accordingly, the dimension of needle failure seemed to be about 200 μm. It is known that polymeric materials under a compressive force exhibit elastic properties in a low strain range, and they undergo failure when the strain increases to a certain degree (i.e., yield point) (Ebewele 2000; Ward and Sweeney 2012). It could be suggested that the failure load of MN0 was found to be about 0.4018 N because the elastic deformation was terminated around that value. The third strain observed after 200 μm of strain occurred would be an elastic deformation because the
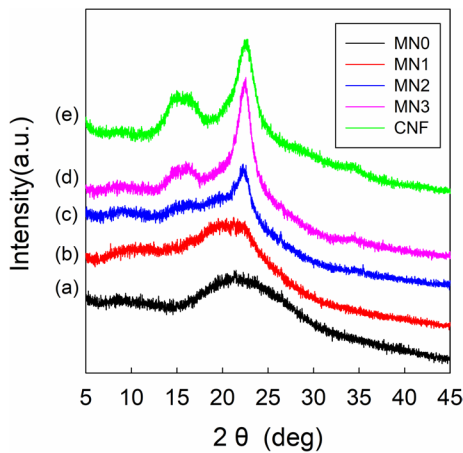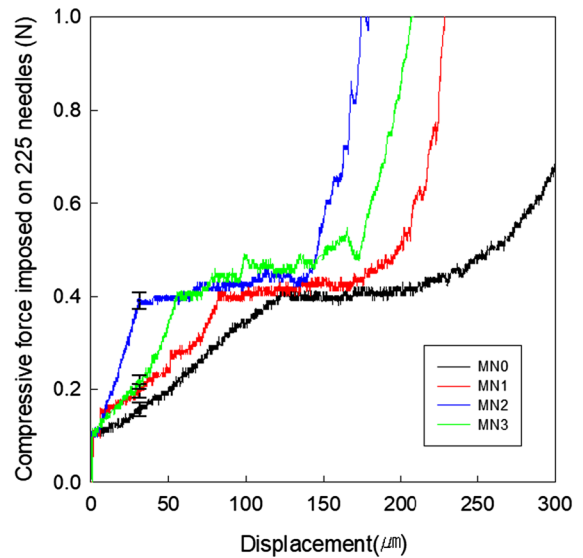
Fig. 4 XRD spectrum of MN0 (**a**), MN1 (**b**), MN2 (**c**), MN3 (**d**), and CNF (**e**). In the spectrum of CNF, MN2, and MN3, diffraction peaks corresponding to the (110) plane, the (200) plane, and the (004) plane of cellulose crystalline structure were found at 2θ of 15.8°, 22.6°, and 34.4°, respectively

Fig. 5 Compressive force profiles of MN0 (black), MN1 (red), MN2 (blue), and MN3 (green). The first elastic strain is due to the elastic deformation of needle tip, the second non-elastic plateau strain is because of the needle tip failure, and the third elastic strain is attributed to the elastic deformation of the thicker stem under the fractured tip. Considering the curve slope in the first elastic region, the stiffness seemed to be greater in the order of MN2 > MN3 > MN1 > MN0. The experiment was repeated 3 times. The statistical significance evaluated at a displacement (ca. 30 μm) where the needles exhibiting the highest Young's modulus (i.e. MN2) began to undergo their tip failure was as follows. MN0 (black) vs MN1 (red): $p < 0.05$, MN0 (black) versus MN2 (blue): $p < 0.001$, and MN0 (black) vs MN3 (green): $p < 0.01$

compressive force was proportional to the strain. The thicker stem under the fractured tip would still be able to be compressed in an elastic manner.

In the compressive force profile of MN1, compressive force increased up to 0.4116 N almost linearly while the strain increased to 82 μm, it was almost constant in strain range of 82–168 μm, and thereafter it increased again with increasing strain. The failure load of MN1 was about 0.4116 N, close to that of MN0. A notable difference was the compressive force in the elastic deformation region of the tip of MN1 increased more rapidly than that of MN0. This suggests that MN1 was more stiff and brittle than MN0. Even if CNF was contained in MN1 as low as 3.3%, it seemed to provide stiffness to the needles. As described previously, CNF is a bundle of cellulose molecules, and it contains crystalline domains in its structure. Owing to the crystalline domain, CNFs are stiff and would increase the stiffness of the needles. Furthermore, since CNF strands are long (in order of micrometers) enough to be physically entangled, they would undergo a long-range interaction. The hydrogen bonding among CNF strands would also enhance the long-range interaction. In this circumstance, CNF strands would be able to form networks and endow the needles with stiff property.

The compressive force profile of MN2 resembled that of MN1. An obvious difference was that the slope in the first elastic deformation region was much higher than that of MN1. The CNF content of MN2 was 16% and it was about three times higher than that of MN1. Owing to the higher CNF content, the stiffness of CNFs was thought to be more reflected on the mechanical property of MN2. In addition, the higher CNF content would enable CNF networks to be formed more readily and give rise to the production of more stiff needles. Unlike MN1, MN2 exhibited a small but obvious increase in the compressive force between the tip failure and the second elastic deformation. This suggested that the tip failure occurred in a stepwise manner.

Increment in the compressive force between the tip failure and the second elastic deformation became more prominent for MN3. The CNF content of MN3 was 33% which was about 10 times higher than that of MN1. Considering the surface

of MN array was rougher as the CNF content was higher, CNFs seemed to be clustered into their own domain, possibly due to an extensive physical entanglement, especially when its content was high (e.g., 33%). The mass ratio of CNF/HA/collagen was about 1:1:1 when the CNF content was 33%. At such a high content, CNF would hardly form a network of homogenously dispersed strands but form its own domain. In this circumstance, MN3 would exhibit heterogeneous mechanical properties. This could account for why the compressive force in the second deformation region (the tip failure region) increased in a stepwise manner.

The slope of the compressive force profile in the first elastic deformation region of MN3 was lower than that of MN2. The formation of CNF domains was thought to be less favorable in enhancing the stiffness of needles than the formation of a network of homogenously dispersed CNFs, which might be obtained at a moderate CNF content. By taking advantage of the compressive force and the displacement at failure, Young's modulus of the single needle tip of MN0, MN1, MN2, and MN3 were calculated to be 0.286 MPa, 0.446 MPa, 1.202 MPa, and 0.649 MPa, respectively. The Young's moduli were those of the MN tips, not those of the whole MNs. After the tip failed, the stem still underwent elastic deformation without failure (Fig. 5). Since the needle was pyramidal, the average cross-sectional area of the needle was used as the area to which the compressive force was applied. Since 225 (15×15) needles were subjected to the compressive force, the force applied to the single needle tip at failure of MN0, MN1, MN2, and MN3 were calculated to be 1.786×10^{-3} N, 1.830×10^{-3} N, 1.742×10^{-3} N, and 1.786×10^{-3} N, respectively, and they were used for the calculation of Young's modulus.

Figure 6 shows the SEM micrograph of MN0, MN1, MN2, and MN3 after subjected to compressive strength test. All the MN arrays exhibited bent tips but intact stems. The length of tip bending on the SEM micrograph was estimated to be 124–166 μm, and it was in good agreement with the length of tip bending evaluated in the compressive strength test (i.e., strain where the second elastic began to take place, 123–170 μm). The maximum strain (i.e., 300 μm) for the compressive strength test was more than two times higher than the length of tip bending, but the needle stem below the fractured tip remained

intact. This suggested that the needle stem underwent an elastic deformation.

Skin-piercing capability of MNs

Figure 7 shows the micrographs of perforated skins after the application of MN0, MN1, MN2, and MN3. Perforated holes were clearly found on the skins and they were formed due to the penetration of MNs into the skin. After removed from the skin, all the needles remained intact and no needle debris was found on the skin. The perforation degree by MN0, MN1, MN2, and MN3 was 81.8, 97.8, 98.7, and 96.4%, respectively. The skin-piercing capability of the MN arrays with CNF (i.e., MN1, MN2, and MN3) was higher than that of the MN array without CNFs (i.e., MN0).

It was reported that several factors, including the diameter, the geometry, the mechanical property of needles, and the applied compressive force, affected the skin-piercing capability of the MNs (Gittard et al., 2013). The diameter, the geometry, and the applied force were the same among the MN arrays tested, they could be excluded from the factors affecting the skin-piercing capability. As long as the needle failure load was higher than the compressive force applied to the MN array, the stiffness of the needle was thought to be one of major factors affecting the skin-piercing capability. As the stiffness of the needle is higher, it would absorb the applied force less and transfer the force to the skin more efficiently. In fact, the needles of the MN array containing CNFs (i.e., MN1, MN2, and MN3) were stiffer than those of the MN array without CNFs (i.e., MN0) (Fig. 5).

According to a previous work, it was recommended that needles with below 12:1 aspect ratio of length-to-equivalent diameter and more than 3 GPa of Young's modulus should be used for reducing sudden failure by buckling and for successful insertion of the needle into human cadaver skin (Park and Prausnitz 2010). The height of the needle of present study was 600 μm, the average cross-section area was calculated to be 30,000 μm^2, the equivalent diameter was calculated to be 97 μm, thus the aspect ratio of the needle was estimated to be about 6:1, which falls within the proposed criterion (i.e. less than 12:1). The Young's modulus of the tip of single needle containing CNFs was 0.446–1.202 MPa and the values were less than the proposed criterion (i.e. greater than 3 GPa).
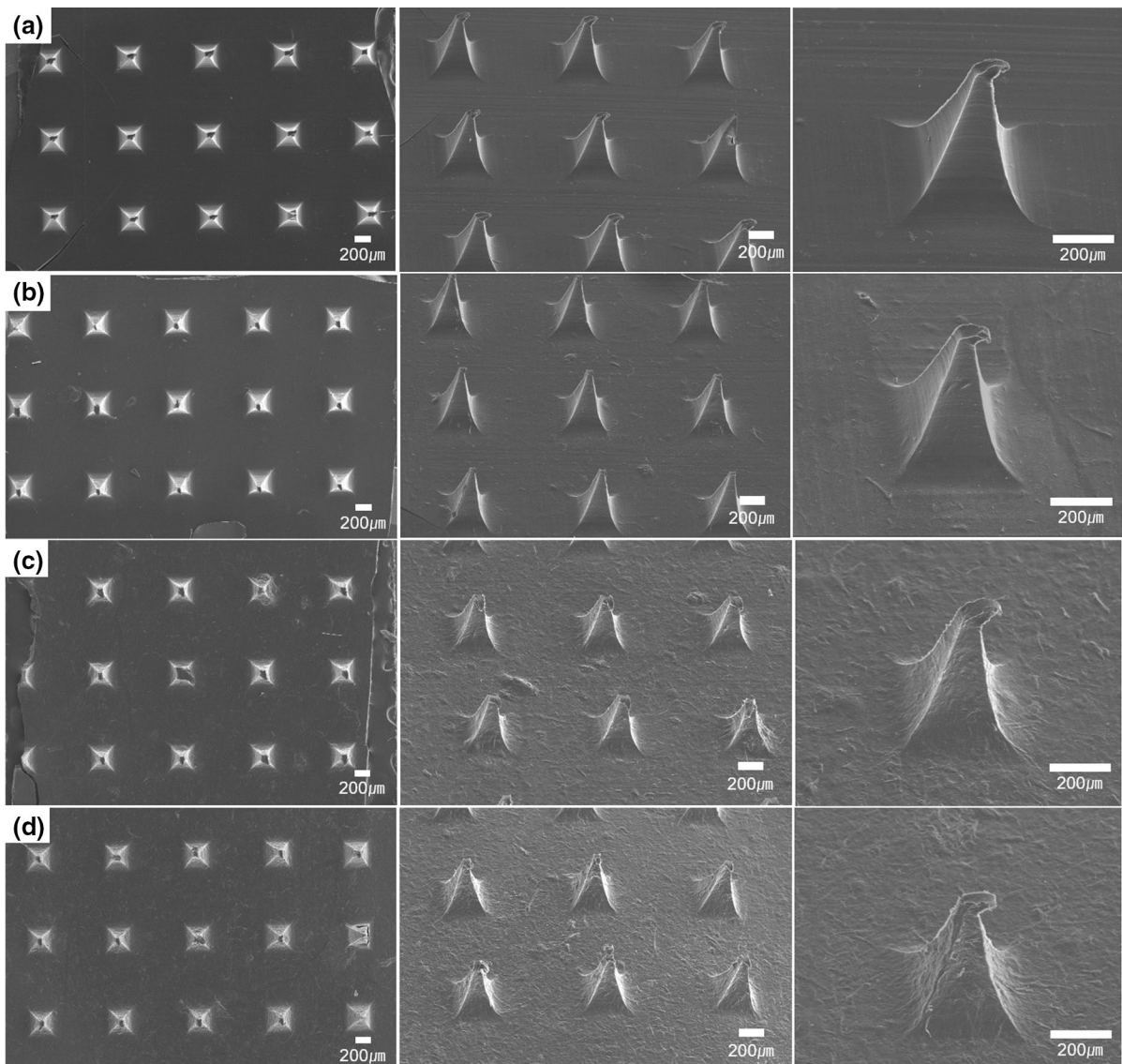
Fig. 6 SEM micrograph of MN0 (**a**), MN1 (**b**), MN2 (**c**), and MN3 (**d**) after subjected to compressive strength test. The force applied to the single needle tip at failure of MN0, MN1, MN2, and MN3 were 1.786×10^{-3} N, 1.830×10^{-3} N, 1.742×10^{-3} N, and 1.786×10^{-3} N, respectively

Nevertheless, under present experimental condition, the skin perforation degrees by the MNs incorporating CNFs (e.g. MN1, MN2, and MN3) were found to be almost 100% and all the needles remained intact after removed from the skin. The criteria for successfully inserting the needle into the skin might change, depending on the needle geometry and the skin origin (human, animal, artificial). In addition, the Young's moduli calculated in this study were those of the tips of the needles, not those of the whole needles. After

the tips were failed, the stems were still subjected to the elastic deformation without failure (Fig. 5).

On the other hand, the force required to penetrate human skin was reported to be 0.08 N/needle (Davis et al. 2004). In the present study, the force imposed on the single needle at tip failure was measured to be 0.0017 to 0.0018 N, far lower than the required force (0.08 N/needle). Thus, the MNs was theoretically likely to undergo their tip failure during skin penetration. However, the yield strengths calculated

**Fig. 7** Photomicrograph of perforated skins after the application of MN0 (**a**), MN1 (**b**), MN2 (**c**) and MN3 (**d**)
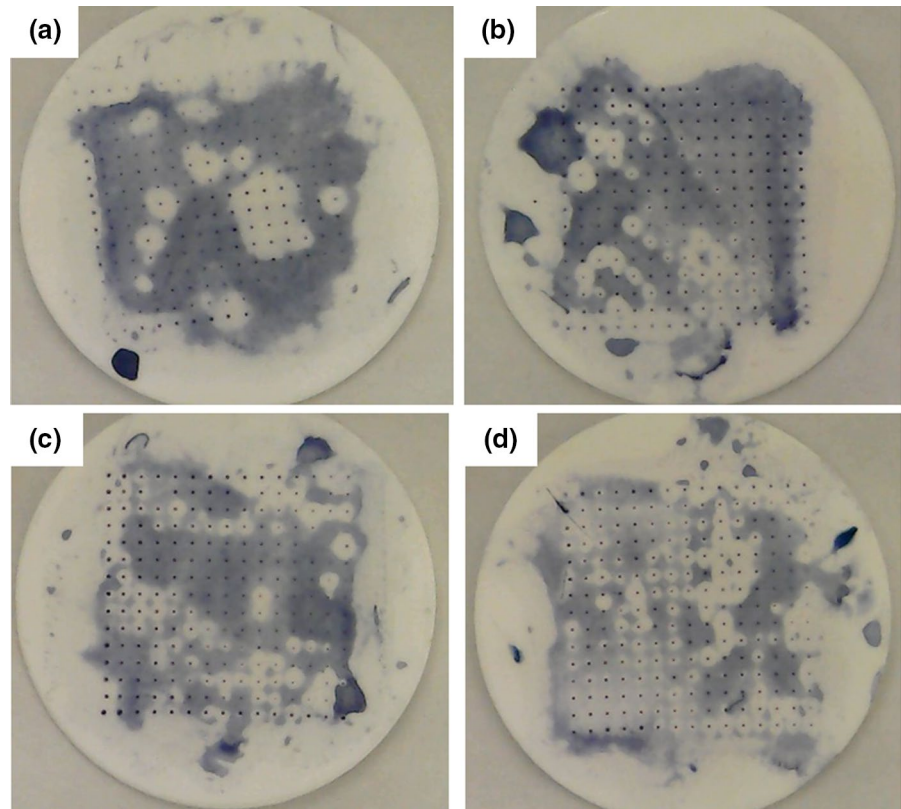
Fig. 8 Black and white micrograph (**a**), fluorescence micrographs (**b**), and combined micrograph (**c**) of cross-section of MN0-attached skin
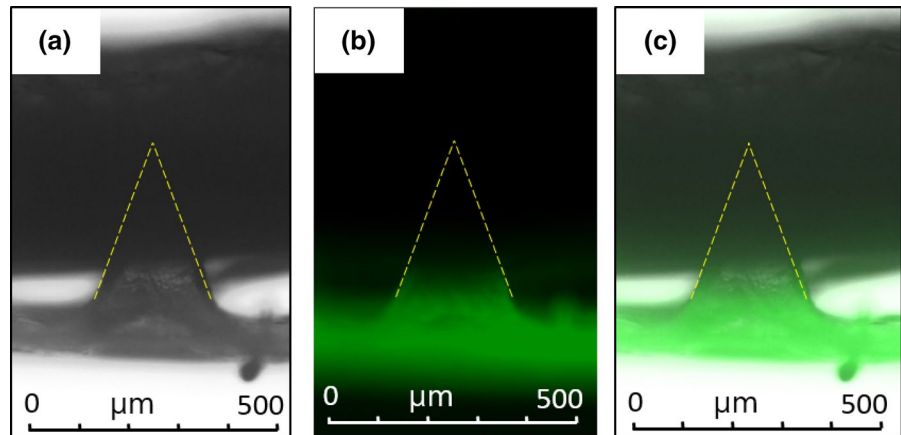
in the present study were those of the tips of the needles, not those of the whole needles. After the tips failed, the stems underwent elastic deformation without failure (Fig. 5). Since our MNs could efficiently penetrate the artificial skin without fracture (Fig. 7), it could be said the MN strength was strong enough to perforate the skin.

Skin penetrating capability of MNs

Figure 8 shows the black and white micrograph, the fluorescence micrograph, and the combined micrograph of the cross-section of MN0-attached skin. On the black and white micrograph, about one-third of the MNs penetrated into the skin. Due to the incomplete penetration, the space between the skin and the
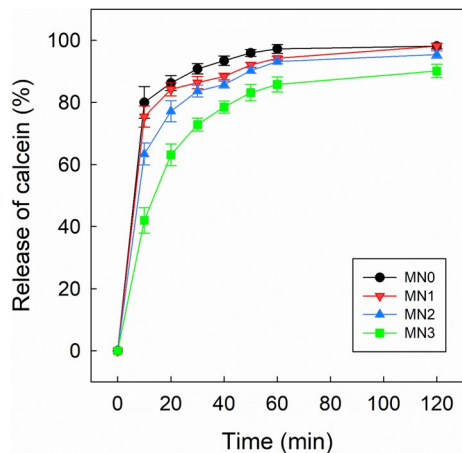
Fig. 9 Release profile of calcein loaded in MN0 (●), MN1 (▼), MN2 (▲), and MN3 (■). Each data point was obtained by 3 times repeated experiments

MN base was observed to be white. On the fluorescence micrograph, the MN array was yellowish-green and the bottom part of a pyramidal needle was found not to penetrate into the skin. On the combined micrograph, the skin was observed to be black and the MN array was yellowish-green. It also exhibited that about one-third of the needle penetrated into the skin and the rest remained out of the skin. The skin penetrating capability of MN arrays containing CNFs (i.e. MN1~3) was not markedly different from that of MN0 (not shown here). The pyramidal needles underwent an elastic deformation after their tips were ruptured (Fig. 5) thus the compressive force applied on the MN arrays would be absorbed by the elastic stems of the needles and not transferred to the skin effectively. This could account for why the MNs could not penetrate into the skin completely.

Release of fluorescence dye from MN array

Figure 9 shows the release profile of calcein loaded in MN0, MN1, MN2, and MN3. The release degree of dye loaded in MN0 increased fast to 86% for the initial 20 min, followed by a slow increase to 98% during the remaining period. The other arrays also exhibited a saturated release profile. Such a saturated release profile was reported when a water-soluble cargo was loaded in a matrix type of vehicle (Gurny et al. 1982). Since the release rate (i.e., the slope of the release curve) decreased with time-lapse, the

release mechanism kinetics seemed to follow 1st order release. The initial release rates were calculated to be 0.996, 0.946, 0.772, and 0.518 mg/min/ml for MN0, MN1, MN2, and MN3, respectively. This indicated that the release rate decreased as the CNF content increased, especially in the early stage. For example, the release degree in 10 min of dye loaded MN0, MN1, MN2, and MN3 were about 80, 75, 63, and 42%, respectively. The difference in the release degree became small as the time-lapse increased, and all the MN arrays exhibited an extensive release degree in the later stage (i.e., more than 90% in 120 min).

MN0 was composed of only water-soluble polymers thus it would be readily dissolved in aqueous solution and release its payload fast because the dissolution would govern the release rate. Whereas, MN1, MN2, and MN3 contained water-insoluble fibers (i.e. CNFs) in their water-soluble polymeric matrix. As described previously, the strands of CNFs would be able to form networks within the MN array owing to their physical entanglement and/or hydrogen bonding among the strands. Thus, the MN array containing CNFs would be less readily dissolved in aqueous solution. In this circumstance, the release would be controlled by not only the dissolution of the matrix but also by the diffusion of dye in the matrix. This may account for why the release rate decreased as the CNF content increased. However, the release degree was more than 90% in 120 min even though the MN array containing CNFs were not fully dissolved and disintegrated. The arrays could easily become swelled and loosened in tens of minutes possibly due to the dissolving out of the water-soluble polymers (i.e., HA and collagen). Thus, the payload (i.e. calcein) was able to be readily leached out of the swelled and loosened arrays.

Figure 10 shows the photographs of MN0 and MN3 in the buffer solution (32 ℃) when time-lapse was 10 min and 24 h. MN0 lost its integrity at 10 min, possibly because HA and collagen (the major components of the MN array) would be readily dissolved in an aqueous solution. Whereas MN3 maintained most of its shape at 10 min, possibly because CNFs would form water-insoluble networks within the MN array. Thus, MN3 would release its payload mainly by a diffusion mechanism in the early stages, which would be a reason why the release degree in the early stage of dye loaded in the MN arrays containing CNFs

Fig. 10 Photomicrograph of MN0 (**a′**) and MN3 (**b′**) in the buffer solution (32 °C) when time lapse was 10 min (**a**) and 24 h (**b**)
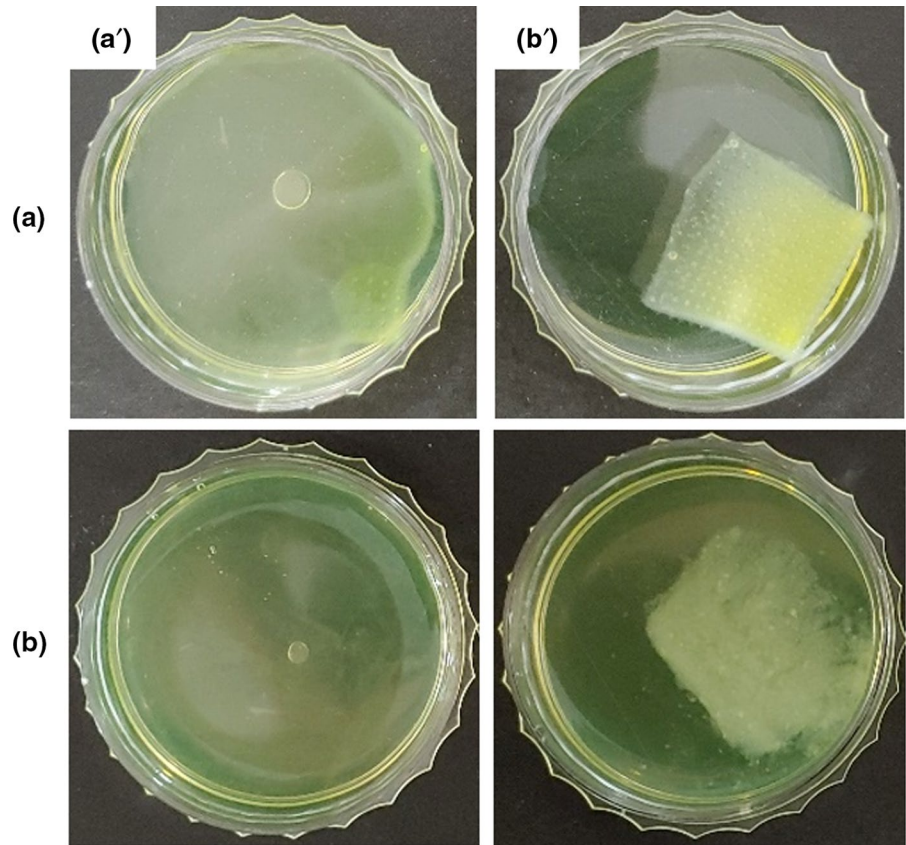
was much lower than that of dye loaded in the MN array without CNFs (Fig. 9). However, at a prolonged time-lapse (i.e., at 24 h), MN0 was completely disintegrated, and MN3 was not completely disintegrated but seemed to be loose and swelled due to the leaching out of the water-soluble polymers (i.e., HA and collagen). In this circumstance, both MN0 and MN3 would release their payload by a dissolution mechanism. This could account for why the difference in the release degree among the MN arrays became small as the time lapse increased, and all the MN arrays exhibited an extensive release degree in the later stage of release.

In vitro skin permeation

Figure 11 shows the cumulative amount of calcein permeated through the skin for 24 h when MN0, MN1, MN2, MN3, and the dye solution were applied to the skin. The cumulative amount of calcein permeated through the skin for 24 h was negligible when the solution was applied to the skin. Calcein is
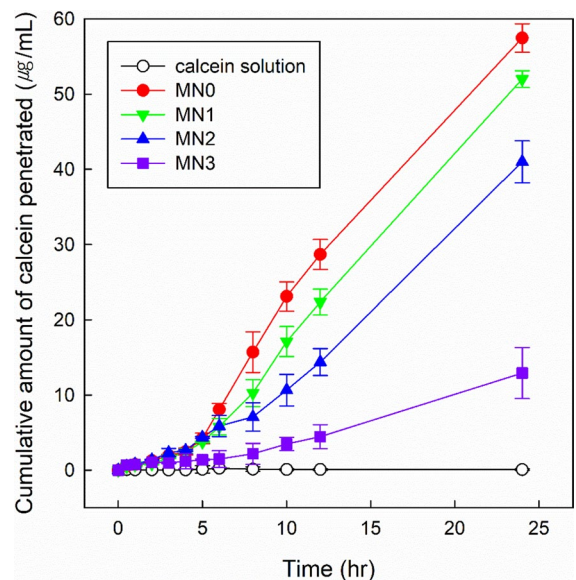
Fig. 11 Cumulative amount of calcein permeated through skin for 24 h when MN0 (●), MN1 (▼), MN2 (▲), MN3 (■), and dye solution (○) were applied onto skin. Each data point was obtained by 3 times repeated experiments

water-soluble and would hardly be partitioned into the skin due to its high polarity. On the other hand, the cumulative amount of dye loaded in the MN array markedly increased with time-lapse. The permeation took place very slowly for the first 5 h and fast during the remaining period. It took hours for the skin to be fully wetted with receptor solution and equilibrated with it, so the MN would be wetted a little or dissolved very slowly in the early stage of skin permeation experiment due to the small amount of absorbed solution. In this circumstance, the dye would be released out of the needles mainly by diffusion, accounting for why the skin permeation took place so slowly in the early stage. Once the skin was fully wetted with receptor solution, the amount of absorbed solution would be enough for the needles to be readily dissolved. Accordingly, the dye would be released mainly by the dissolution of the needles, accounting for why the skin permeation occurred relatively fast in the late stage. The degree of skin permeation was greater in the order of dye loaded in $MN0 > MN1 > MN2 > MN3$. For example, the cumulative amount in 24 h of dye permeated through the skin was 57, 52, 41, and 12 µg/ml, respectively, when the dye was loaded in MN0, MN1, MN2, and MN3. The MN arrays prepared in the present study would deliver the water-soluble compound through the skin in a "poke and release" way because it was a dissolving or a semi-dissolving type of needle. "Poke"-related factors affecting the skin permeation would be the skin-piercing degree and the skin penetration depth of needles. "Release"-related factors would be the diffusion rate of a payload in the needles and the dissolving rate of the needles. The skin-piercing capability of the MN arrays containing CNFs (i.e., MN1~3) was a little higher than that of the MN array containing no CNFs (i.e., MN0). Thus, the former MN arrays would be more favorable in enhancing the skin permeation of the payload only if the skin-piercing capability is concerned. Regardless of the type of MN array, the needles could not thoroughly pierce the skin and could only partially penetrate into the skin even though the length of the MNs (about 600 µm) was two times longer than the thickness of the skin (about 300 µm), possibly because the needles were elastic and would absorb the compressive force applied on the MN array. Theoretically, as the MNs were stiffer, they would absorb less compressive force and could deeply penetrate into the skin. However,

the size of the pierced holes formed on the skin was almost the same (Fig. 7), suggesting almost similar skin penetration depth. The factors affecting the diffusion rate of a payload in the needles would be the compactness and the polarity of the MN array and the interaction between the payload and the MN array (e.g., electrostatic and hydrogen bonding). The MN arrays were dissolved or disintegrated if they were immersed in an aqueous solution during a prolonged time period (e.g., 24 h, Fig. 10). Thus, in long-term skin permeation, the factors affecting the diffusion would be negligible and the dissolution would dominate the release of the payload from the needles and seemed to be a major factor affecting the skin permeation. In fact, the MN array without CNFs (i.e. MN0) that exhibited the highest skin permeation was readily solubilized and the MN array containing the highest CNF content (i.e. MN3) that showed the lowest skin permeation was not readily disintegrated. In conclusion, the skin permeation of a cargo loaded in the dissolving MN array was controlled by adjusting CNF content thus the dissolving rate.

For practical use, the needles penetrated into the skin should be soluble because the MN array is aiming at either dermal or transdermal delivery but the base needs to be insoluble to maintain the array integrity. Even if the base is soluble, it would not matter because it can hardly be dissolved if the body fluid of the skin surface (e.g. epidermal water and sweat) is little. In fact, however, MN arrays studied in present work are a continuous array, they provide an occlusive condition when applied to the skin, and prevent the epidermal water loss, causing an excess skin water content. Sweat would also be accumulated under the occlusive condition. Due to the high humidity under a MN array, not only the needles but also the base would be solubilized and release its cargo, thus the amount of a payload permeated through the skin would be higher than obtained with a dry skin. The release of a payload from the base also needs to be taken into an account when a MN array is designed for dermal/transdermal delivery in case excess moisture is developed under the MN array. If sweat is secreted in excess due to an exercise, etc., it would be able to dissolve the MN array partly and even disintegrate it. In order to retard the dissolution and prevent the disintegration, additives including CNFs may be required to be included in the array. By the way, the dose obtained the microneedle matrix

would not markedly change regardless of whether the skin is wet. A payload released from the needles can easily be absorbed by a skin because it hardly encounters the absorption barrier served by the stratum corneum once the needles have penetrated into the skin. Whereas, a payload released from the base would suffer from a low skin absorption due to the absorption barrier of the stratum corneum. The skin permeation amount would be mainly dominated by a payload released from the needles but not by a payload released from the base. Thus, the dose would not fluctuate markedly under variable skin conditions. On the other hand, a constant dose can be achieved by preventing the release of a payload from the base. One of methods to prevent the release from the base and deliver a consistent dose would be to layer over an impermeable membrane onto the base surface. Another method would be to build microneedles on an insoluble base by filling the pores of the mold with soluble materials for the formation of microneedles then layering over them with insoluble materials. The components comprising the MN array of present study are hyaluronic acid, collagen, trehalose, and CNFs and all of them are known to be biocompatible, so they would hardly do harm to human body. Insulin, human growth hormone, antisense for gene therapy, mRNA vaccines, epidermal growth factor, botulinum toxin, etc. can be delivered dermally or transdermally using the MN array developed in this study.

Conclusions

Dissolving MN arrays of different CNF contents (0, 3.3, 16, and 33%) were fabricated by casting the mixture solutions of CNF, HA, collagen, and trehalose on the surface of PDMS molds and drying them at room temperature. The base width (ca. 300 μm) and the height (ca. 600 μm) of the polymeric needles of MN arrays were the same as those of the metallic needles of a master, confirmed on a SEM microscope. In the compressive strength test, the needles were found to become more stiff upon including CNFs in MN array. The elastic deformation of the tip, the failure of the tip, and the elastic deformation of stem took place in turn, and the stems of needles remained intact with the tips bent. MN arrays containing CNFs exhibited a higher skin-piercing capability than a MN array without CNFs, which would be ascribed to the stronger

stiffness of needles containing CNFs. The release rate of a water-soluble dye (i.e. calcein) from MN arrays decreased as the CNF content increased, possibly because CNF strands would interact with one another through physical entanglement and/or hydrogen bonding, form networks within the MN arrays, and fall the dissolution rate of the needle down. The in vitro skin permeation of the cargo loaded in MN arrays also decreased as the CNF content increased. The dissolution rate of the needles seemed to govern the transdermal delivery rate. CNFs would be able to be used as a controller for the stiffness of the needles, the dissolving rate of the needles, thus the skin permeation rate of a cargo loaded in the needles.

Declarations

Conflict of interest The authors declare no conflicts of interest.

Ethical approval This article does not contain any studies with human participants or animals performed by any of the authors.

References

Benson HAE, Grice JE, Mohammed Y et al (2019) Topical and transdermal drug delivery: from simple potions to smart technologies. Curr Drug Deliv 16:444–460. https://doi.org/10.2174/1567201816666190201143457

Cha KJ, Kim T, Park SJ, Kim DS (2014) Simple and cost-effective fabrication of solid biodegradable polymer microneedle arrays with adjustable aspect ratio for transdermal drug delivery using acupuncture microneedles. J Micromec Microeng. https://doi.org/10.1088/0960-1317/24/11/115015

Chen W, Yu H, Liu Y et al (2011) Individualization of cellulose nanofibers from wood using high-intensity ultrasonication combined with chemical pretreatments. Carbohydr Polym 83:1804–1811. https://doi.org/10.1016/j.carbpol.2010.10.040

Daddona PE, Matriano JA, Mandema J, Maa Y-F (2011) Parathyroid hormone (1–34)-coated microneedle patch system: clinical pharmacokinetics and pharmacodynamics for treatment of osteoporosis. Pharm Res 28:159–165. https://doi.org/10.1007/s11095-010-0192-9

Davis SP, Landis BJ, Adams ZH et al (2004) Insertion of microneedles into skin: measurement and prediction of insertion force and needle fracture force. J Biomech 37:1155–1163. https://doi.org/10.1016/j.jbiomech.2003.12.010

Dufresne A (2017) Cellulose nanomaterial reinforced polymer nanocomposites. Curr Opin Colloid Interface Sci 29:1–8. https://doi.org/10.1016/j.cocis.2017.01.004

Ebewele RO (2000) Polymer science and technology. CRC Press

Fularz A, Almohammed S, Rice JH (2022) Metal-free cellulose-based platforms for biomolecule fluorescence signal enhancement. ACS Sustain Chem Eng 10:508–520. https://doi.org/10.1021/acssuschemeng.1c06995

Gittard SD, Chen B, Xu H et al (2013) The effects of geometry on skin penetration and failure of polymer microneedles. J Adhes Sci Technol 27:227–243. https://doi.org/10.1080/01694243.2012.705101

Gurny R, Doelker E, Peppas NA (1982) Modelling of sustained release of water-soluble drugs from porous, hydrophobic polymers. Biomaterials 3:27–32. https://doi.org/10.1016/0142-9612(82)90057-6

Jeong H-R, Kim J-Y, Kim S-N, Park J-H (2018) Local dermal delivery of cyclosporin A, a hydrophobic and high molecular weight drug, using dissolving microneedles. Eur J Pharm Biopharm 127:237–243. https://doi.org/10.1016/j.ejpb.2018.02.014

Jiang X, Lillehoj PB (2020) Microneedle-based skin patch for blood-free rapid diagnostic testing. Microsys Nanoeng 6:96. https://doi.org/10.1038/s41378-020-00206-1

Kim JA, Park SC, Alle M et al (2021) Magnesium ascorbyl phosphate loaded in dissolving stiff microneedles containing cellulose nanofiber. J Drug Deliv Sci Technol 63:102439. https://doi.org/10.1016/j.jddst.2021.102439

Kiziltas A, Nazari B, Kiziltas EE et al (2016) Cellulose NANOFIBER-polyethylene nanocomposites modified by polyvinyl alcohol. J Appl Polym Sci. https://doi.org/10.1002/app.42933

Koutsonanos DG, Compans RW, Skountzou I (2013) Targeting the skin for microneedle delivery of influenza vaccine. Adv Exp Med Biol 785:121–132. https://doi.org/10.1007/978-1-4614-6217-0_13

Kozlov PV, Burdygina GI (1983) The structure and properties of solid gelatin and the principles of their modification. Polymer (guildf) 24:651–666. https://doi.org/10.1016/0032-3861(83)90001-0

Kumar A, Singh Negi Y, Choudhary V, Kant Bhardwaj N (2020) Characterization of cellulose nanocrystals produced by acid-hydrolysis from sugarcane bagasse as agro-waste. J Mater Phys Chem 2:1–8. https://doi.org/10.12691/jmpc-2-1-1

Lee JW, Park J-H, Prausnitz MR (2008) Dissolving microneedles for transdermal drug delivery. Biomaterials 29:2113–2124. https://doi.org/10.1016/j.biomaterials.2007.12.048

Mittapally S, Taranum R, Parveen S (2018) Microneedles-a potential transdermal drug delivery. Int J Pharma Res Heal Sci 6:2579–2585

Ossowicz-Rupniewska P, Nowak A, Klebeko J et al (2021) Assessment of the effect of structural modification of ibuprofen on the penetration of ibuprofen from pentravan®(Semisolid) formulation using human skin and a transdermal diffusion test model. Materials 14:6808. https://doi.org/10.3390/ma14226808

Park J-H, Prausnitz MR (2010) Analysis of mechanical failure of polymer microneedles by axial force. J Korean Phys Soc 56:1223–1227. https://doi.org/10.3938/jkps.56.1223

Park J-H, Allen MG, Prausnitz MR (2005) Biodegradable polymer microneedles: Fabrication, mechanics and transdermal drug delivery. J Control Release 104:51–66. https://doi.org/10.1016/j.jconrel.2005.02.002

Prausnitz MR (2004) Microneedles for transdermal drug delivery. Adv Drug Deliv Rev 56:581–587. https://doi.org/10.1016/j.addr.2003.10.023

Quinn HL, Kearney M-C, Courtenay AJ et al (2014) The role of microneedles for drug and vaccine delivery. Expert Opin Drug Deliv 11:1769–1780. https://doi.org/10.1517/17425247.2014.938635

Sharma S, Hatware K, Bhadane P et al (2019) Recent advances in microneedle composites for biomedical applications: Advanced drug delivery technologies. Mater Sci Eng C 103:109717. https://doi.org/10.1016/j.msec.2019.05.002

Sullivan SP, Murthy N, Prausnitz MR (2008) Minimally invasive protein delivery with rapidly dissolving polymer microneedles. Adv Mater 20:933–938. https://doi.org/10.1002/adma.200701205

Tejado A, Alam MN, Antal M et al (2012) Energy requirements for the disintegration of cellulose fibers into cellulose nanofibers. Cellulose 19:831–842. https://doi.org/10.1007/s10570-012-9694-4

van der Maaden K, Jiskoot W, Bouwstra J (2012) Microneedle technologies for (trans)dermal drug and vaccine delivery. J Control Release 161:645–655. https://doi.org/10.1016/j.jconrel.2012.01.042

Waghule T, Singhvi G, Dubey SK et al (2019) Microneedles: a smart approach and increasing potential for transdermal drug delivery system. Biomed Pharmacother 109:1249–1258. https://doi.org/10.1016/j.biopha.2018.10.078

Wang L, Gardner DJ, Bousfield DW (2018) Cellulose nanofibril-reinforced polypropylene composites for material extrusion: Rheological properties. Polym Eng Sci 58:793–801. https://doi.org/10.1002/pen.24615

Ward IM, Sweeney J (2012) Mechanical properties of solid polymers. Wiley

Xu B, Wu XY, Ling SQ et al (2013) Fabrication of 3D metal micro-mold based on femtosecond laser cutting and micro-electric resistance slip welding. Int J Adv Manuf Technol 66:601–609

Ye Y, Yu J, Wen D et al (2018) Polymeric microneedles for transdermal protein delivery. Adv Drug Deliv Rev 127:106–118. https://doi.org/10.1016/j.addr.2018.01.015

Yin Z, Kuang D, Wang S et al (2018) Swellable silk fibroin microneedles for transdermal drug delivery. Int J Biol Macromol 106:48–56. https://doi.org/10.1016/j.ijbiomac.2017.07.178

Zaupa A, Neffe AT, Pierce BF et al (2010) A molecular dynamic analysis of gelatin as an amorphous material: prediction of mechanical properties of gelatin systems. Int J Artif Organs 34:139–151. https://doi.org/10.5301/IJAO.2010.6083